

# Magnetic Levitation Camera Robot for Endoscopic Surgery

Massimiliano Simi, *Student IEEE*, Gianluca Sardi, Pietro Valdastri, *Member IEEE*, Arianna Menciassi, *Member IEEE*, Paolo Dario, *Fellow IEEE*

**Abstract** - A wired miniature surgical camera robot with a novel Magnetic Levitation System (MLS) was modeled, designed and fabricated. A simple analysis and a theoretical model were developed in order to describe and predict basic behavior for different structural parameters of the system. The robot is composed of two main parts (head and tail) linked by a thin elastic flexible joint. The tail module embeds two magnets for anchoring and manual rough translation. The head module incorporates two motorized donut-shaped magnets and a miniaturized vision system at the tip. The MLS can exploit the external magnetic field to induce a smooth bending of the robotic head, guaranteeing a high span tilt motion of the point of view ( $0^{\circ}$ - $80^{\circ}$ ). The device is 100 mm long and 12.7 mm in diameter. Use of such a robot in single port or standard multiport laparoscopy could enable reduction of number/size of ancillary trocars, and/or increase the number of working devices that can be deployed, thus paving the way for multiple point of view laparoscopy.

## I. INTRODUCTION

Conventional laparoscopic surgery reduces pain in the patient and facilitates postoperative recovery by using small multiple abdominal incisions where different instruments are inserted. In the continuous quest to limit access trauma, Single Port Laparoscopy (SPL) is concretely emerging from research into clinical practice [1]. SPL procedures utilize conventional as well as angled and articulating instrumentation introduced through a multilumen port (25-30 mm in diameter) placed, normally, in the patient navel. In addition to the clear cosmetic benefits, other possible advantages of SPL surgery compared with conventional laparoscopy include less postoperative pain, faster recovery, less adhesion formation, and reduction of convalescence time [2-4]. However, SPL procedures are significantly hampered by limited instrument triangulation capabilities (i.e. the two surgical instruments and the endoscope are close to each other), narrow visual field through conventional laparoscopes, and both internal and external tool collisions that can considerably limit surgeon performance and jeopardize the patient's safety.

A softly-tethered camera system that can be steered from the outside of the abdomen and that is able to provide a "stadium" view, i.e. a view from above the surgical field as defined in [5], would solve most of the open issues of SPL. Additionally, if the camera size is compatible with standard

laparoscopic trocars, the access used for inserting the robot can be used for a different instrument afterwards, thus avoiding a dedicated trocar for the videoendoscope.

A number of preliminary devices have been developed towards this goal. In particular, monocular devices exploiting magnetic fixation and manual motion are reported in [5, 6]. In order to guarantee a finer control, large or complex robotic camera systems with active internal degrees of freedom have been proposed [7, 8]. Our research group has previously developed a very small (12.7 mm in diameter, 32 mm in length) robotic camera magnetically driven with one internal degree of freedom (DoF), based on an innovative Magnetic Internal Mechanism (MIM) [9, 10]. All these prototypes, however, present many different drawbacks related to large size, poor stability, reliability and motion range, or scarce maneuvering.

In this paper, the authors present a novel wired camera prototype, with a robotic internal active Magnetic Levitation System (MLS). Based on the concept known as Magnetic Anchoring and Guidance System (MAGS) [11-13], the small robotic magnetic levitation endoscope is intra-abdominally moved or anchored by External Permanent Magnets (EPMs) placed on the abdominal skin. After a rough positioning, the main benefit derives from the innovative MLS, that exploits the external magnetic field and an internal actuator to guarantee a wide-range precise robotic tilt motion of the camera.

Furthermore, the thin flexible cable, which guarantees robot powering and real time signal transmission, leaves the access port almost free, thus allowing the insertion of an additional tool. Additionally, such a tether allows for an effective retrieval of the device in case of failure.

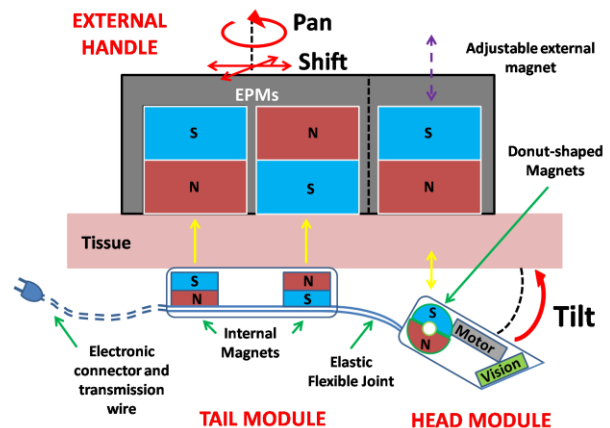


Fig.1 Schematic representation of the entire robotic endoscope with the MLS. The interaction between internal and external magnets and the 4 related degrees of freedom are underlined by yellow and red arrows respectively.

Manuscript received September 15, 2010. This work was supported in part by European Commission in the framework of the ARAKNES European Project EU/IST-2008-224565.

All the authors are with the BioRobotics Institute, Scuola Superiore Sant'Anna, Pisa, Italy.

M. S. is the corresponding author (phone: +39 050 883483; fax: +39 050 883497; e-mail: m.simi@sssup.it.)

The next section describes the MLS concept, and illustrates the main parts of the robot. Section III presents a brief analysis and a simple model aimed at describing basic system behavior and the robotic prototype with MLS dimensioning. The development and fabrication of the first prototype is reported in Section IV, while conclusions are reported in Section V.

## II. PRINCIPLE OF OPERATION

As represented in Fig.1, the proposed surgical platform is composed by the wired robotic endoscope with MLS and an external handle embedding 3 permanent magnets. The robotic camera is composed by two modules, the head and the tail, connected together by a flexible joint. The head embeds the vision system and a couple of donut-shaped and diametrically magnetized magnets that can be rotated by an internal brushless motor. The tail hosts a couple of permanent magnets that, once coupled with the external ones, provides anchoring and stability to the robot. In addition to coarse manual maneuvering (3 DoFs, i.e. pan and planar translation), allowed by the magnetic link between external and on-board magnets, the concept of MLS exploits the internal actuator to generate a variable magnetic field, thus allowing for a wide-range controlled bending of the head module. Attractive or repulsive magnetic forces can be exerted on the robot head thanks to the complete rotation ( $360^\circ$ ) of the donut-shaped magnets and in principle, this allows to achieve a  $90^\circ$ -wide tilt motion of the camera point of view. To effectively implement robot head levitation an equilibrium among weight force, flexible joint stiffness and magnetic force must be guaranteed for the complete range of operation (magnetic torque is neglected for the sake of simplicity), as illustrated in the section below.

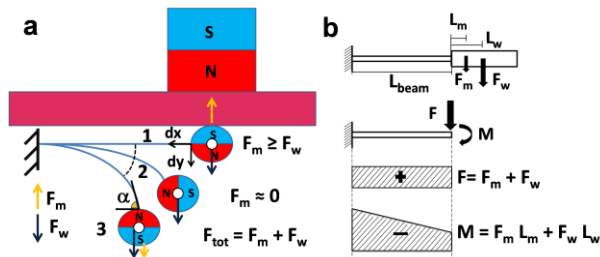


Fig. 2 a). Schematic representation of MLS operation. In the equilibrium point (2) the magnetic force is negligible b). Force analysis and distribution considering the flexible joint like an isotropic homogeneous linear elastic beam and the head as a non-deformable body.  $L_w$  and  $L_m$  are the distances from the beam tip to the centre of gravity and the centre of donut-shaped magnets respectively.  $L_{beam}$  is the beam length.

## III. SYSTEM ANALYSIS

### A. Magnetic Anchoring and Translation System Modeling

Based on the MAGS principle [11-13], some simple considerations allow to evaluate what happens during magnetic anchoring and external motion, and the requirements that our system must meet. In particular, the magnetic attraction force between the external permanent

magnets embedded in the handle and the magnets inside the tail module must always be stronger than the robotic endoscope weight force (neglecting repulsive magnetic force on the head module and clockwise momentum on tail tip) in order to guarantee a stable anchoring.

The static friction force that is always opposite to the robot motion (pan and translation) is directly dependent on the vertical magnetic attraction force and the static friction coefficient of the tissue. The motion of both EPMS represents the worst condition for maintaining stable anchoring, thus if we consider a plane translation of the EPMS, the friction force falls proportionally to the vertical magnetic attraction whereas the horizontal component grows. When the horizontal magnetic force component overcomes the friction force, the endoscopic robot follows the EPMS. Thus, in order to provide motion to the robot (pan and translation) and maintain reliable anchoring, two conditions must be met at the same time. The horizontal magnetic force component must overcome the static friction force, while the waning vertical attraction force must always overcome the weight force. In Section IV several system parameters are defined and these requirements are quantitatively evaluated (see also Fig.5 and Fig.6).

### B. Magnetic Levitation System Analysis

A more sophisticated analysis must be performed for a proper dimensioning of the MLS. As first step, the following assumptions must be made to facilitate modeling. The tail frame is considered as rigidly anchored to a crushproof layer of tissue. Additionally, the flexible joint is assumed as a homogeneous and isotropic linear elastic beam, fixed at one side and subjected to two different forces (weight  $F_w$  and magnetic force  $F_m$ ) on the other side. Given this, three basic configuration define the behavior of the MLS, i.e. as the donut-shaped magnets rotate, the magnetic force can have either the same (Fig. 2a - 3) or the opposite (Fig. 2a - 1) orientation of the weight force, or it can be negligible (Fig. 2a - 2).

We refer to this last configuration as equilibrium point and it represents the static condition defined as equilibrium between weight force and beam stiffness. Correct operation of the MLS must always guarantee sufficient magnetic attraction to lift the robot head from the equilibrium point to the  $0^\circ$  tilt position (1), whereas the repulsive magnetic force can give an extra span deformation by pushing down the head from the equilibrium to the maximum tilt angle (3).

To correctly describe the flexible joint deformation behavior it is important to define other specific MLS features. In particular, the weight force is assumed as acting at the head module centre of gravity, while the magnetic force acts on the donut-shaped magnets and not on the joint side. However, if we consider the head module as a non-deformable body, the two forces can be supposed to be applied at the connection between the flexible joint and the module, providing their respective momentum in the same point (Fig. 2b).

Equations (deriving from the Euler-Bernoulli model) can be applied to describe the deformation of a linear elastic isotropic beam, providing information about the distal

(camera) side displacement and the bending angle [14-16]. Our main requirement was to guarantee a sufficient magnetic force to lift the head from the equilibrium point to the 0° tilt configuration. In order to maximize the camera tilt span angle, we reach the largest bending angle for an equilibrium point where the magnetic force still overcomes the head module weight force (assuming only the donut-shaped magnets oriented as in Fig.2a-1).

Starting from the boundary condition of concentrated force and momentum at the free tip respectively:

$$\left. \frac{d^2y}{dx^2} \right|_{L=L_{\text{beam}}} = 0 \quad \text{and} \quad \left. \frac{d^3y}{dx^3} \right|_{L=L_{\text{beam}}} = \frac{F}{EJ} \quad (1)$$

$$\left. \frac{d^3y}{dx^3} \right|_{L=L_{\text{beam}}} = 0 \quad \text{and} \quad \left. \frac{d^2y}{dx^2} \right|_{L=L_{\text{beam}}} = \frac{ML}{EJ} \quad (2)$$

we derived the simple equations below (3-9) to describe the distal side displacement ( $dx$  and  $dy$ ) and the bending angle ( $\alpha$ ) for the equilibrium point ( $0 < L < L_{\text{beam}}$ ), considering force and momentum contributions (Fig. 2b):

$$\alpha_F = \frac{FL^2}{2EJ} \quad (3)$$

$$dy_F = \frac{FL^3}{3EJ} \quad (4)$$

$$dx_F = \frac{2EJ}{LF} \sin(\alpha_F) \quad (5)$$

$$\alpha_M = \frac{ML}{EJ} \quad (6)$$

$$dy_M = \frac{EJ}{M}(1 - \cos(\alpha_M)) \quad (7)$$

$$dx_M = \frac{EJ}{M} \sin(\alpha_M) \quad (8)$$

$$\begin{cases} dx = dx_F + dx_M \\ dy = dy_F + dy_M \\ d\alpha = d\alpha_F + d\alpha_M \end{cases} \quad (9)$$

The subscripts  $F$  and  $M$  define the force or momentum contribution to the beam deflection.  $E$  is the beam Young's modulus,  $J$  is the beam moment of inertia,  $L$  represents a generic location along the beam and  $F$  and  $M$  are the concentrated force and moment respectively.

As regards system design, the features of the head module were determined by the functional components embedded in it, e.g. camera and illumination, motor and mechanism, donut-shaped magnets. On the other end, the features of the tail module were designed to satisfy the requirements discussed in Section IIIA. Given this, the remaining free parameter for maximizing the head module span is the flexible joint. In the next Sections we applied the model to predict the equilibrium point and the related span angle as function of flexible joint features.

## IV. ROBOT PROTOTYPE DESIGN AND FABRICATION

### A. External Permanent Magnets

Since the EPMs must be easily handled by the medical doctor, and on the basis also of our main technical guidelines (external magnetic field maximization), three off-the-shelf (KJ Magnetics, Jamison U.S.) cubic (25.5 mm x 25.5 mm x 25.5 mm) magnets (NdFeB, N52) were selected as best compromise between high magnetic field and size, to generate the external magnetic field both for the MAGS and the MLS. Two of them were embedded in the same plastic handle separated by a 3 mm wall, whereas the third (for the MLS) was fixed in a specific metallic chassis linked to the handle by means of a mechanism that allows for vertical translation. This adjustment allows to achieve the optimal equilibrium position (Fig. 2a-2) for different wall thicknesses. In the current platform, this adjustment is performed by a trial and error procedure. In the final version of the system, a magnetic field sensor will be embedded in the head module.

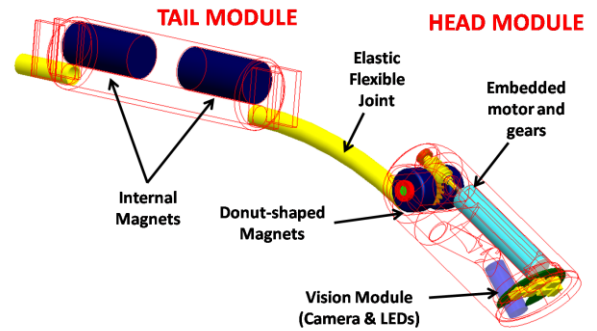


Fig.3 Tridimensional model of the designed prototype. The head module embeds ring magnets, a motor with gears and a vision system; the tail module only two magnets for the system anchoring and external rough motion.

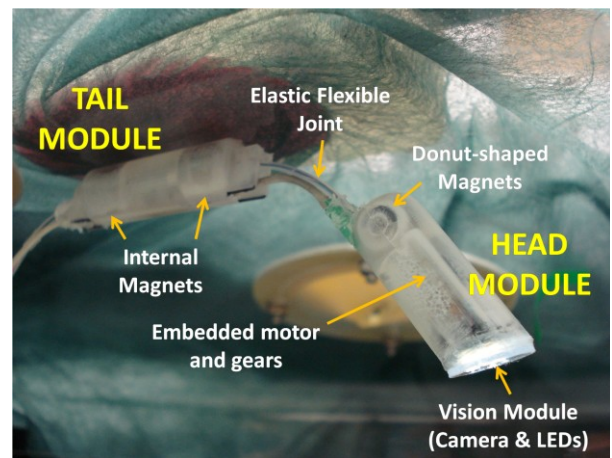


Fig.4 The fabricated MLS endoscopic robot prototype. The two modules are linked by an elastic PTFE sheath that protect the wires. The camera cable runs in parallel to the flexible joint.

## B. Head Module

Considering the endoscopic camera robot described in [9], a very similar prototype was fabricated as head module of the new robot. An improvement regarded orientation of the camera sight direction with an angle of  $20^\circ$ . The head modules (Fig. 3 and Fig. 4) consists of a small and light plastic cylinder (12.7 mm in diameter, 34 mm in length and 7.5 g in weight, fabricated by rapid prototyping) that embeds two donut-shaped magnets (6.3 mm and 1.6 mm in external and internal diameter respectively and 3.2 mm in thickness) diametrically magnetized (NdFeB, N52) and linked by means of two gears (worm and helical gears) to a brushless motor (SBL04-0829-PG337 Namiki precision Jewel Co. Ltd., Tokyo, Japan). It also includes a VGA vision system composed of a thin endoscopic camera (STORZ, CCD 500x582) and a set of high efficiency white LEDs (NESW007BT, Nichia Corp., Tokushima, Japan ) for illumination. Dedicated experimental tests demonstrated that the interference between the 6 V supplied brushless motor and the internal and external magnetic fields surrounding the robot head (35 mT) are negligible [17].

Several soft and thin wires were required to connect the device to the power supply and to allow for real time delivery of the images. They also provided effective retrieval from the abdomen especially in case of failure. An external push-button console was used for activating the internal motor and defining the rotation of the donut-shaped magnets. In stepping mode the motor can be driven with a resolution of  $0.2^\circ$ . This translates in a tilt resolution of  $0.01^\circ$ .

## C. Tail Module

The tail module is 11 mm in diameter, 40 mm in length and 10.5 g in weight (see Fig.3 and Fig.4). It was designed to satisfy the requirements discussed in Section IIIA. Given the geometry and the properties of the EPMS, two commercially available (KJ Magnetics, Jamison U.S.) cylindrical (6.35 mm in diameter and 12.7 in length) magnets (NdFeB, N52) were embedded in the tail. A long longitudinal hole in the frame body allowed the wires to run through the module. Considering average human abdominal wall thickness as 30 mm [18], the magnetic attraction forces between internal and external magnets were evaluated using Finite Element Method (FEM) analysis (COMSOL MULTIPHYSICS 3.4, Sweden). All properties of the magnets, such as magnetic permeability  $\mu_0 = 1.05$  and different geometric dimensions, were set into the simulations. Keeping the position of the tail magnets fixed, we derived the trends of horizontal ( $F_{mx}$ ) and vertical ( $F_{my}$ ) magnetic forces and defined a discrete horizontal EPMS displacement of 2.5 mm in a range from 0 to 15 mm (Fig. 5).

The total weight of the robotic endoscope, including both head and tail modules, is 18 g, thus a minimum  $F_{my}$  of 176 mN ( $F_{ion}$ ) is required to lift and anchor the device. Once the force trend was obtained, the static friction force ( $F_f$ ) opposing to the tail motion was calculated as a function of the vertical magnetic attraction, considering the weight of the entire robot and the static friction coefficient ( $\mu$ ) of the internal abdominal tissue as  $10^{-1}$  [19].

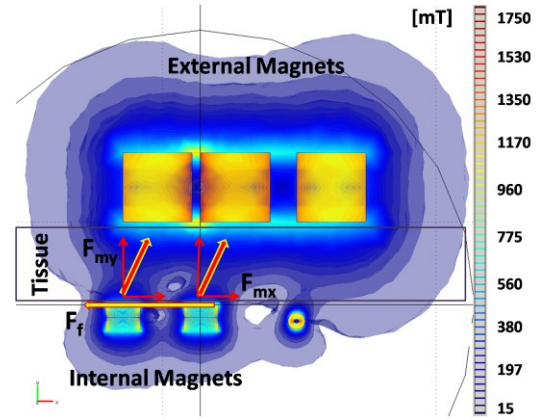


Fig.5 FEM analysis of the magnetic interaction between tail internal magnets and the EPMS in order to evaluate magnetic force components ( $F_{mx}$  and  $F_{my}$ ). The selected mesh consisted of 1,300,000 elements with a minimum quality ratio of 0.34. The EPMS and tail magnets are 12.5 mm shifted along the x direction.

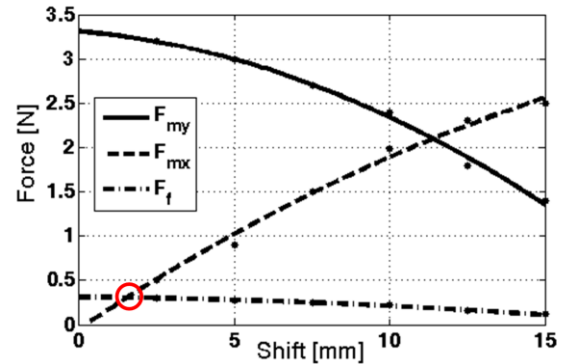


Fig.6 Plot of the magnetic attraction forces ( $F_{xm}$  and  $F_{ym}$ ) and the derived friction force ( $F_f = (F_{my} - F_{ion}) \cdot \mu$ ) occurring between tail magnets and EPMS as function of the EPMS translation. The discrete simulations result as dots. The circle highlights the intersection between  $F_{mx}$  and  $F_f$  trends.

$F_{mx}$  must overcome the friction force, while  $F_{my}$  is higher than the total weight force of the robot. As shown in Fig. 6, the vertical force drops with the displacement as well as  $F_f$ . On the other hand,  $F_{mx}$  grows with the displacement and the trend line overcomes the  $F_f$  line for a horizontal displacement of about 2 mm where the vertical magnetic attraction is still very high (more than 3 N), thus guaranteeing very stable anchoring also during the planar motion of the entire robot (see the companion video [20]).

## D. Flexible Joint

The flexible joint is the last and more complex part to dimension in order to obtain optimal MLS functioning.

After defining the head module features in terms of geometry, weight and magnetic content, and the external magnet properties we decided to evaluate MLS behavior related to different elastic joint length.

Due to the presence of wires between the two robotic modules (tail and head), we decided to put the wires into an elastic polytetrafluoroethylene (PTFE) sheath (1.5 mm in diameter) that served as elastic flexible joint.

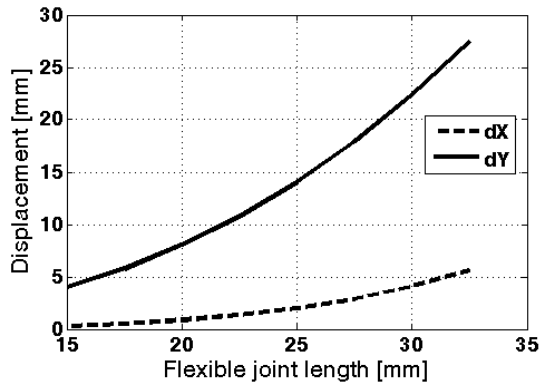


Fig. 7 Plot of the equilibrium point displacement ( $dx$  and  $dy$ ) as function of the flexible joint length with a defined robot head and beam properties.

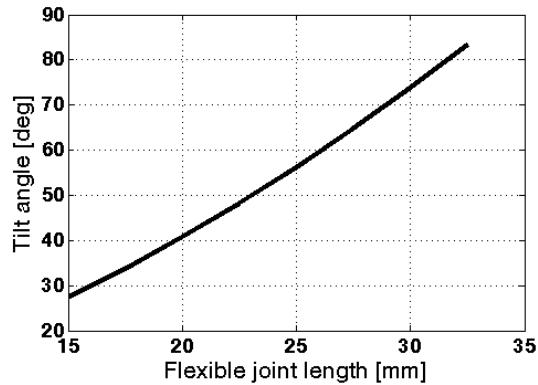


Fig. 8 Plot of the deformation angle ( $\alpha$ ) at the beam tip for the equilibrium point as function of the beam length with a defined head weight and beam properties.

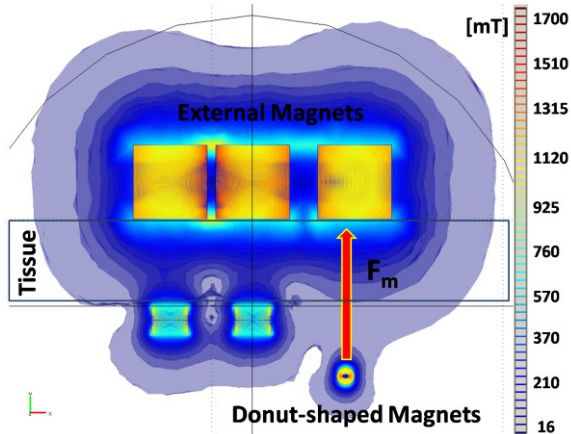


Fig. 9 FEM analysis of the magnetic interaction between donut-shaped magnets and the external magnets in order to evaluate magnetic force components ( $F_m$ ) for different equilibrium points. The selected mesh consisted of 1,300,000 elements with a minimum quality ratio of 0.34. Equilibrium point for a  $L_{beam}$  equal to 27.5 mm.

The total joint elastic module ( $E$ ) was experimentally evaluated as 200 MPa with a negligible plasticity and hysteresis. It is worth mentioning that in this first prototype the camera cable runs in parallel to the flexible joint, however its stiffness is negligible with respect to the PTFE sheath, therefore it was not considered during system design. In future prototypes it will be included in the sheath.

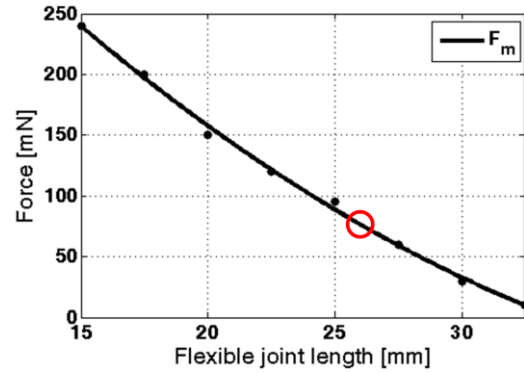


Fig. 10 Trend line of the vertical magnetic attraction force between the MLS external and donut-shaped magnets in equilibrium point (Fig. 2a-2). The dots represent the discrete FEM analysis results. The circle highlights the  $F_m$  equal to  $F_w$  for a 26 mm  $L_{beam}$ .

Based on the known parameters ( $F_w = 73.5 \text{ mN}$ ;  $L_w = 14 \text{ mm}$ ;  $J = 2.5 \cdot 10^{-13} \text{ mm}^4$ ;  $E = 200 \text{ MPa}$ ), and considering equations (3-9), the trend lines of the equilibrium point, in terms of  $dx$  and  $dy$  displacement, and the relative bending angle ( $\alpha$ ), were obtained as function of the beam length ( $L_{beam}$ ) (Fig. 7 and Fig. 8).

Discrete FEM analysis was used to evaluate the vertical magnetic attraction force between the donut-shaped magnets positioned as function of the relative beam tip equilibrium point (but assumed oriented as in Fig. 2a-1) and the external magnet, for each different beam length (from the highest angle to the lowest with  $L_{beam}$  step of 2.5 mm) (Fig. 9). The values of magnetic field and the magnetic attraction force obtained with simulations were also experimentally verified with a magnetometer (KOSVAHA 5, Wuntronic, Germany) and a load cell (Nano17, ATI, U.S.) as in [9], respectively.

Based on the obtained plot (Fig. 10) a beam length of 26 mm defined the highest bending angle and still guaranteed a magnetic force ( $F_m = 80 \text{ mN}$ ) sufficient to lift the head module from the equilibrium point. An angle of  $60^\circ$  was reached in the equilibrium point whereas an angle of  $80^\circ$  was reached if we also included the magnetic repulsion force. Once the flexible joint had been assembled to the other two robotic modules, the MLS was tested. The tilt angles were measured elaborating lateral views of the robot placed on a millimeter-scaled background. The test demonstrated, as predicted, a total smooth and fine tilt span ranging from  $0^\circ$  up to  $80^\circ$  in relation to the surrounding tissue as showed in Fig. 11 and in the companion video [20].

## V. CONCLUSION

The MLS represents a novel concept to obtain a reliable, fine and smooth internal DoF for a robotic camera device immersed in a magnetic field. The authors demonstrate the feasibility of this approach by designing and fabricating a first working prototype. It is 12.7 mm in diameter, 100 mm in length and 18 g in weight. It is composed of two robotic modules (tail and head) linked by an elastic flexible joint. Under a set of conditions, detailed above, when the embedded motor is activated, the robot head module can levitate, thus tilting the on-board camera with a span ranging from  $0^\circ$  to  $80^\circ$  (Fig. 11).

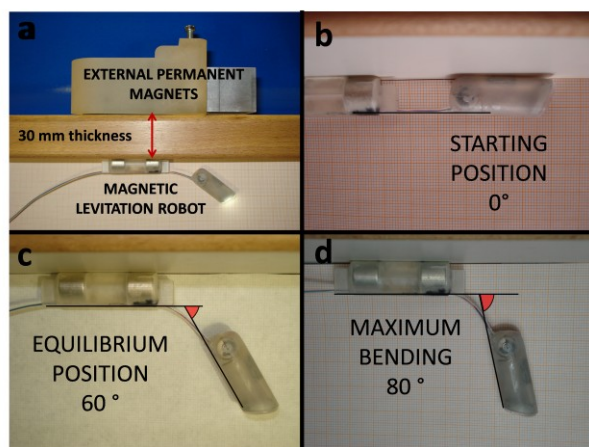


Fig.11 Evaluation of the tilt span a). Test scenario b). The maximum attraction force keeps the robot head near the abdominal wall. c). Equilibrium position:  $F_m$  is negligible and the head tilt angle is  $60^\circ$ . d) The repulsive magnetic force pushes down the head that reaches a final angle of  $80^\circ$ .

The small robotic endoscope can be inserted through a conventional trocar and fixed on the abdominal wall. Space in the access port is only taken by thin cables (1.5mm), thus leaving free space for the access of additional instrumentation. A rough position along the abdominal wall can be achieved by dragging the robot with the motion of the EPMS. Once positioned, a fine robotic tilt orientation of the camera can be obtained by exploiting only the MLS. Accordingly, the novel robotic endoscope has the potential to restore triangulation for the surgeon and to reduce both instrument collision and procedure invasiveness. In laparoscopy, use of this innovative approach would reduce the number of external incisions, since a devoted access for the camera would no longer be required. Considering an SPL scenario, all the ports can be used to insert instruments, thus facilitating the surgeon and also eliminating the potential conflict with the endoscopist. Moreover, multiple camera robots can be introduced through one incision, thus providing the surgeon with multiple points of view of the surgical arena. Multiple points of view combined with robotic camera steering may potentially enable three-dimensional reconstruction of the abdominal cavity, to be presented to the surgeon through augmented reality techniques [21, 22].

Preliminary in vivo tests performed on a porcine model demonstrated all the benefits described above and the feasibility of the approach in a real surgical scenario (see the companion video [20]).

Further tests will be performed to completely evaluate system performance, especially as regards the innovative MLS concept. A dedicated control algorithm will be implemented to precisely relate the donut shaped magnets rotation to the head-camera tilt angle.

#### ACKNOWLEDGMENT

The authors wish to thank N. Funaro and C. Filippeschi for prototypes manufacturing and S. Caccavaro for his technical support on the flexible joint analysis.

#### REFERENCES

- [1] Romanelli JR, Earle DB, Single-port laparoscopic surgery: an overview. *Surgical Endoscopy* 2009 Jul; 23(7):1419-1427.
- [2] Raman JD, Bensalah K, Bagrodia A et al (2007) Laboratory and clinical development of single keyhole umbilical nephrectomy. *Urology* 70(6):1039-1042
- [3] Rane A, Rao P, Bonadio F, Rao P (2007) Single port laparoscopic nephrectomy using a novel laparoscopic port (R-Port) and evolution of single laparoscopic port procedure (SLIPP). *J Endourol* 21(1):A287
- [4] Ponsky LE, Cherullo EE, Sawyer M, Hartke D (2008) Single access site laparoscopic radical nephrectomy: initial clinical experience. *J Endourol* 22:663-666
- [5] Swain P, Austin R, Bally K, Trusty R, Development and testing of a tethered, independent camera for notes and single-site laparoscopic procedures. *Surgical Endoscopy* (2010), 24:2013-2021.
- [6] Cadeddu J, Fernandez R, Desai M, Bergs R, Tracy C, Tang S, Rao P, Scott S, Novel magnetically guided intra-abdominal camera to facilitate laparoendoscopic single-site surgery: initial human experience. *Surgical Endoscopy*, 2009, 23: 1894-1899.
- [7] Lehman A, Berg K, Dumpsert J, Wood N, Visty A, Rentschler M, Platt S, Farritor S, Oleynikov D, Surgery with cooperative robots. *Computer Aided Surgery*. 2008, 13: 95-105.
- [8] Hu Y, Allen P, Hongle N, Fowler D, Insertable surgical imaging device with pan, tilt, zoom, and lighting. *Journal of Robotic Research*. 2009, 28:1373-1386.
- [9] Simi M, Ciuti G, Tognarelli S, Valdastrì P, Menciassi A, Dario P, Magnetic link design for a robotic laparoscopic camera, *Journal of Applied Physics*, 2010. (107), 09B302, pp.1-3.
- [10] Valdastrì P, Quaglia C, Buselli E, Arezzo A, Di Lorenzo N, Morino M, Menciassi A, Dario P. A magnetic internal mechanism for precise orientation of the camera in wireless endoluminal applications. *Endoscopy* 2010; 42:481-486.
- [11] Park S, Bergs RA, Eberhart R et al (2007) Trocar-less instrumentation for laparoscopy: magnetic positioning of intraabdominal camera and retractor. *Ann Surg* 245(3):379-384
- [12] Zeltser IS, Cadeddu JA (2008) A novel magnetic anchoring and guidance system to facilitate single trocar laparoscopic nephrectomy. *Curr Urol Rep* 9(1):62-64
- [13] Zeltser IS, Bergs R, Fernandez R et al (2007) Single trocar laparoscopic nephrectomy using magnetic anchoring and guidance system in the porcine model. *J Urol* 178(1):288-291
- [14] Wang J, Chena J, Liaob S. An explicit solution of the large deformation of a cantilever beam under point load at the free tip. *Journal of Computational and Applied Mathematics*. 212:320-330. 2008
- [15] Belendez T, Neipp C, Belendez A. Large and small deflections of a cantilever beam. *European Journal of Physic*. 23;3:371-979. 2002
- [16] Kopmaz O, Gundogdu O. On the curvature of an Euler-Bernoulli beam. *International Journal of Mechanical Engineering Education*, 31/2:132-142.
- [17] M. Simi, P. Valdastrì, C. Quaglia, A. Menciassi, P. Dario "Design, Fabrication and Testing of a Capsule with Hybrid Locomotion for Gastrointestinal Tract Exploration" in *IEEE/ASME Trans. Mechatronics*, vol. 15, pp. 170-180, 2010.
- [18] Song C, Alijani A, Frank T, Hanna G, Cuschieri A. Mechanical properties of the human abdominal wall measured in vivo during insufflation for laparoscopic surgery. *Surgical Endoscopy*, 20:987-990, 2006.
- [19] Loring S, Brown R, Gouldstone A, Butler J, Lubrication regimes in mesothelial sliding. *Journal of Biomechanics*, 2005, 38:2390-2396.
- [20] The Official ARAKNES Project website (Video available online, February 2011) - <http://www.araknes.org/prototypes.html>
- [21] Stoyanov D, Scarzanella MV, Pratt P, Yang GZ (2010) Real-time stereo reconstruction in robotically assisted minimally invasive surgery. *Med Image Comput Assist Interv* 13(Pt 1):275-282
- [22] Lee SL, Lerotic M, Vitiello V, Giannarou S, Kwok KW, Visentini-Scarzanella M, Yang GZ (2010) From medical images to minimally invasive intervention: Computer assistance for robotic surgery. *Comput Med Imaging Graph* 34:33-45.